

Effect of probe geometry during measurement of >100 A Ga_2O_3 vertical rectifiers

Cite as: J. Vac. Sci. Technol. A **39**, 013406 (2021); <https://doi.org/10.1116/6.0000815>

Submitted: 24 November 2020 . Accepted: 01 December 2020 . Published Online: 21 December 2020

 Ribhu Sharma, Minghan Xian,  Chaker Fares, Mark E. Law,  Marko Tadjer, Karl D. Hobart,  Fan Ren, and  Stephen J. Pearton

COLLECTIONS

Paper published as part of the special topic on [Gallium Oxide Materials and Devices](#)



[View Online](#)



[Export Citation](#)



[CrossMark](#)

ARTICLES YOU MAY BE INTERESTED IN

[A review of \$\text{Ga}_2\text{O}_3\$ materials, processing, and devices](#)

Applied Physics Reviews **5**, 011301 (2018); <https://doi.org/10.1063/1.5006941>

[Perspective: \$\text{Ga}_2\text{O}_3\$ for ultra-high power rectifiers and MOSFETS](#)

Journal of Applied Physics **124**, 220901 (2018); <https://doi.org/10.1063/1.5062841>

[Near-ideal reverse leakage current and practical maximum electric field in \$\beta\text{-Ga}_2\text{O}_3\$ Schottky barrier diodes](#)

Applied Physics Letters **116**, 192101 (2020); <https://doi.org/10.1063/5.0007715>





Advance your science and career as a member of

AVS

[LEARN MORE](#) 

Effect of probe geometry during measurement of >100 A Ga₂O₃ vertical rectifiers

Cite as: J. Vac. Sci. Technol. A 39, 013406 (2021); doi: 10.1116/6.0000815

Submitted: 24 November 2020 · Accepted: 1 December 2020 ·

Published Online: 21 December 2020



Ribhu Sharma,¹  Minghan Xian,² Chaker Fares,²  Mark E. Law,¹ Marko Tadjer,³  Karl D. Hobart,³ Fan Ren,²  and Stephen J. Pearton^{4,a)} 

AFFILIATIONS

¹Department of Electrical and Computer Engineering, University of Florida, Gainesville, Florida 32611

²Department of Chemical Engineering, University of Florida, Gainesville, Florida 32611

³U.S. Naval Research Laboratory, 4555 Overlook Ave SW, Washington, DC 20375

⁴Department of Materials Science and Engineering, University of Florida, Gainesville, Florida 32611

Note: This paper is part of the Special Topic Collection on Gallium Oxide Materials and Devices.

a)Electronic mail: spear@mse.ufl.edu

ABSTRACT

The high breakdown voltage and low on-state resistance of Schottky rectifiers fabricated on β -Ga₂O₃ leads to low switching losses, making them attractive for power inverters. One of the main goals is to achieve high forward currents, requiring the fabrication of large area (>1 cm²) devices in order to keep the current density below the threshold for thermally driven failure. A problem encountered during the measurement of these larger area devices is the dependence of current spreading on the probe size, resistance, number, and geometry, which leads to lower currents than expected. We demonstrate how a multiprobe array (6 × 8 mm²) provides a means of mitigating this effect and measure a single sweep forward current up to 135 A on a 1.15 cm² rectifier fabricated on a vertical Ga₂O₃ structure. Technology computer-aided design simulations using the FLOODS code, a self-consistent partial differential equation solver, provide a systematic insight into the role of probe placement, size (40–4120 μ m), number (1–5), and the sheet resistance of the metal contact on the resultant current-voltage characteristics of the rectifiers.

Published under license by AVS. <https://doi.org/10.1116/6.0000815>

I. INTRODUCTION

Ga₂O₃ is an ultrawide bandgap semiconductor that is attracting attention for power electronics applications.^{1–10} The stable β -polytype has a bandgap of \sim 4.8 eV, a high breakdown field in the range 6–8 MV/cm, and is relatively well-developed in terms of bulk and epitaxial growth and n-type doping capability.^{1–10} While the thermal conductivity is lower than for GaN and SiC, there may be an application space for high current Schottky rectifiers that can be heterogeneously integrated with Si superjunctions or SiC switches in inverter units and more generally in power devices to regulate the flow and conversion of electricity.^{11–36} The Baliga figure of merit for power devices depends on the critical breakdown field to the third power, and this critical field scales as roughly the bandgap (E_G) to the 1.9 power,³⁷ so it is clear that increasing the bandgap can really improve the potential for high power performance.

One notable potential market is inverters for electric vehicles.^{2,3,8,9,11} Others include uninterruptible power supplies,

inverters for photovoltaic systems, power supplies for servers, and charging stations for a range of products, including electric vehicles.^{2,3,8,9,11} Even higher power density and operational temperature and voltage capabilities may allow for power electronics to drive future electrification and next generation power grids.¹¹ Electricity accounts for \sim 38% of primary energy consumption in the U.S. and is the fastest growing form of end-use energy.¹¹ Power electronics play a significant role in the delivery of this electricity in the control and conversion of electrical power to achieve optimal transmission, distribution, and load-side consumption. The fraction of electricity processed through some form of power electronics is estimated to be \sim 80% by 2030, a doubling over the current value.³⁷ Advances in power electronics have the potential for enormous energy efficiency improvements. While power devices based on wide-bandgap semiconductors, such as SiC and GaN, offer enhanced performance for many applications, even higher powers can be achieved with the ultrawide bandgap materials. The switching

electronics for future grid applications needs to achieve currents >100 A.¹¹

Vertical rectifiers are required in order to achieve high absolute switching currents.^{17,26,38–43} The evolution of Ga_2O_3 Schottky vertical rectifiers has seen a move from unterminated devices on bulk substrates to the use of thick epitaxial drift regions, followed by trench structures to enhance the breakdown voltage and then to large area device arrays with forward currents above 30 A under single sweep conditions.^{8,9,17,27} The α -polytype of Ga_2O_3 has an even larger bandgap (~ 5.3 eV),⁵ but the device results reported to date lag behind those with the β -polytype.^{44–47} Oda *et al.*⁴⁴ reported Schottky barrier diodes of corundum-structured gallium oxide with on-resistance of $0.1 \text{ m}\Omega \text{ cm}^2$ grown by mist epitaxy. Kaneko *et al.*⁴⁵ also reported rectifiers on corundum-structured α - Ga_2O_3 . Another often mentioned issue with Ga_2O_3 is the absence of p-type doping, but this is not a major drawback for rectifiers because the inversion time constant is so large at this bandgap and there are few mobile holes due to acceptor trap or impact ionization and the flat valence band. The small amount of stored charge leads to low switching losses.

Besides high forward current and good reverse breakdown voltage (V_{BD}), it is important to achieve low on-state resistance (R_{ON}), which determines system efficiency and thermal loss.^{1–4,8,9,11,37} The on-resistance consists of contributions from the contact resistance, drift region resistance, and the substrate resistance. The latter is minimized by using a heavily doped substrate, while the contact resistance is minimized by techniques such as doping under the contact using implantation, plasma exposure, or annealing.^{8,9,48–50} A recent analysis suggests that $R_{\text{ON}} \sim V_{\text{BD}}^2 E_G^{-5.58}$ for power switches.³⁷

In this paper, we describe the effect of measurement probe size, number, and spacing on the performance of large area ($\sim 1 \text{ cm}^2$), high current (single sweep up to 135 A) Ga_2O_3 rectifiers and how these must be taken into account to reveal the true I-V characteristics.

II. EXPERIMENT

The device structure and fabrication of large area rectifiers has been described in detail previously,^{17,26} but in brief, the starting material was a 2-in. diameter Sn-doped ($n = 3.6 \times 10^{18} \text{ cm}^{-3}$) β - Ga_2O_3 substrate with (001) orientation, $650 \mu\text{m}$ thick, with a $10 \mu\text{m}$ Si doped ($2.3 \times 10^{16} \text{ cm}^{-3}$) epitaxial drift layer grown on top of this by halide vapor phase epitaxy. This gives a range of breakdown voltages from >1 kV for small area devices (contact diameter $\sim 100 \mu\text{m}$) to ~ 300 V for large devices ($\sim 1 \text{ cm}^2$) used for the high current measurements. The origin of reverse leakage current in these types of structures has been assigned to electric field crowding at small voids, with a typical width and depth of 300 and 83 nm, respectively, below the Schottky barrier contact on the Ga_2O_3 surface.⁵⁰ There is no clear relationship between the leakage current path and dislocations present in the initial substrate.⁵⁰

A full area Ti (400 nm)/Au (100 nm) backside Ohmic contact was formed by annealing at 550°C under N_2 . A bilayer dielectric of 40 nm of Al_2O_3 and 360 nm of SiN_x was used for the field plate. These layers were deposited using a Cambridge-Nano-Fiji atomic layer deposition and Plasma-Therm plasma enhanced chemical vapor deposition system, respectively. Field-plates with different

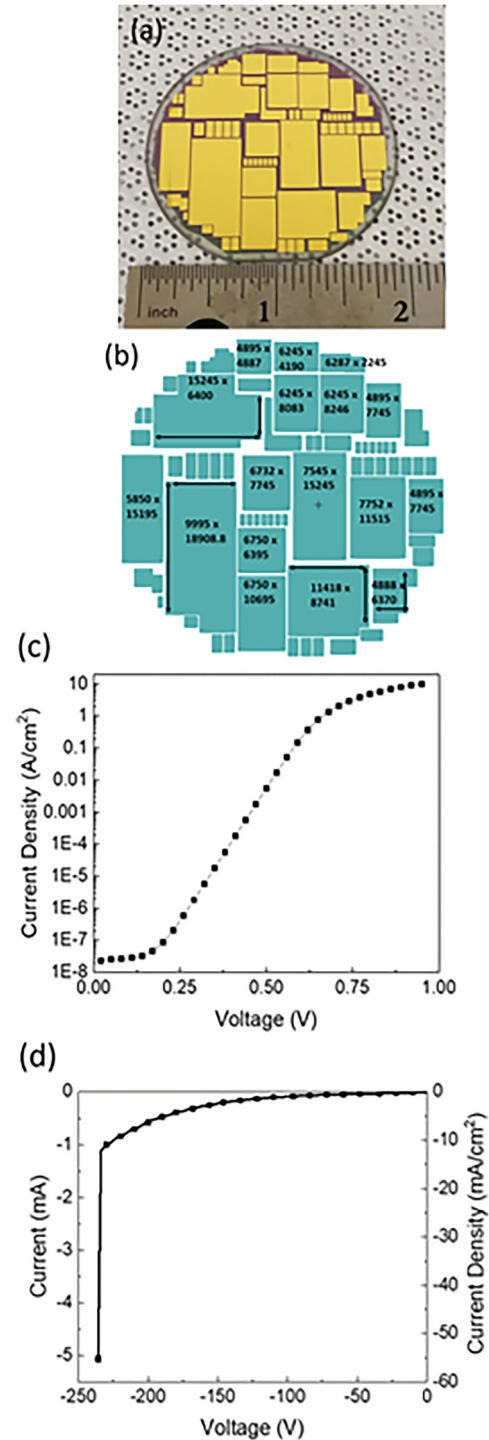


FIG. 1. Optical images of (a) fabricated rectifiers on-wafer, showing a range of areas from 0.035 to 1.89 cm^2 . (b) Map of individual device sizes, listed in micrometers. (c) Forward I-V of rectifier with area 1.15 cm^2 . (d) Reverse I-V of rectifier with area 1.15 cm^2 .

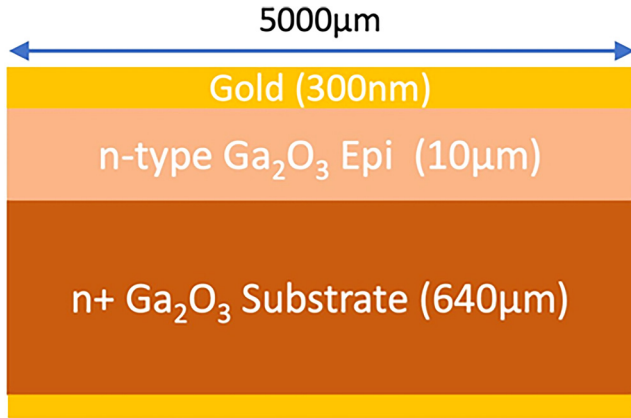


FIG. 2. Schematic of the simulated β -Ga₂O₃ Schottky diode.

sized windows were opened, and an 80 nm thick W (40 nm)/Au (40 nm) Schottky contact was deposited by sputtering deposition followed by 500 °C annealing for 5 min under N₂ to reduce leakage current. 450 nm thick Ti (300 nm)/Au (150 nm) contact was deposited by e-beam evaporation on top of W/Au contact and patterned using standard photolithography to thicken the Schottky contact in order to reduce spreading resistance. The contact area of the resulting rectifiers varied from 0.035 to 1.89 cm². A microscope image of the completed wafer is shown in Fig. 1(a), with a map of the various individual devices and their sizes (in micrometers) shown in Fig. 1(b). The single sweep current-voltage (I-V) characteristics were measured in air at 25 °C on an Agilent 4145B parameter analyzer and a 4284A Precision LCR Meter. For reverse voltages >100 V and forward currents >100 mA, a Tektronix 370 A curve tracer was used due to the rating limits of the Agilent analyzer. A variety of probes were used for the I-V measurements, including spring-mounted Al rods with diameter 3175–6350 μm (0.3175–0.635 cm) and a 6 × 8 array of 0.35 mm Au-tipped stainless-steel probes (area 48 mm²).

The FLOODS TCAD tool⁵¹ is used to generate a comprehensive overview of how the measurement probe setup affects the performance of the Ga₂O₃ rectifiers. A 2D device structure is created and the device equations are initialized in FLOODS, which solves the partial differential equations using the Newton method and discretizes them in space using the finite element method.^{51,52} A simple schematic of the device is given in Fig. 2, where the n-type β -Ga₂O₃ ($N_d = 1 \times 10^{16}$ cm⁻³) epitaxial layer is grown on a highly

TABLE I. Electrical conductivities and the typical range Schottky barrier height of the contact metals used in the simulation.

Contact metal	Electrical conductivity (S/m)	Schottky barrier height (eV)
Gold	4.11×10^7	0.98–1.71
Nickel	1.43×10^7	0.8–1.54
Tungsten	1.79×10^7	0.91

doped n + β -Ga₂O₃ substrate (3.6×10^{18} cm⁻³) with a device diameter of 5000 μm. In order to simulate the thermionic emission at the metal-semiconductor interface, the required boundary conditions have been applied at the top contact (Schottky) and bottom

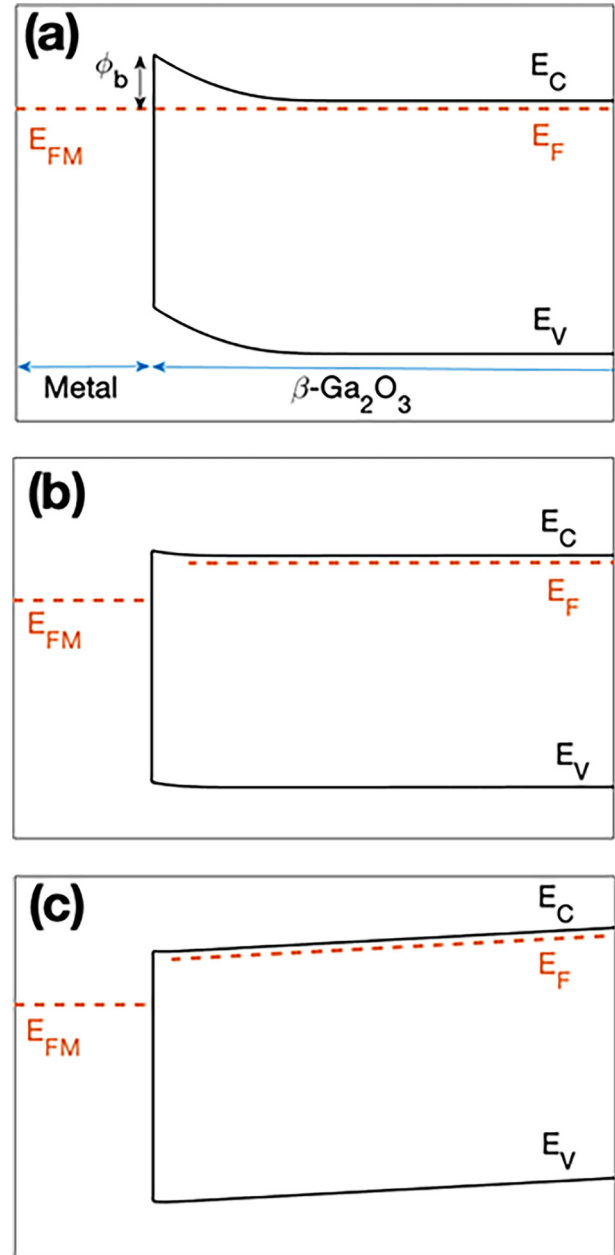


FIG. 3. Simulated band structure of the metal/ β -Ga₂O₃ interface during (a) equilibrium, (b) moderate forward bias, and (c) large forward bias. The larger the slope of the conduction band, the higher is the current flux into the metal.

contact (Ohmic). The top contact metal is considered to be a 300 nm thin gold layer while the Schottky barrier height (ϕ_b) is 1.04 eV. The Schottky barrier height was compared to the experimental values obtained from the slope of the linear region of the forward I-V characteristics.⁵³

The probe contact is also defined to take into account the structural variations of the measurement probe setup and the side-walls have a reflective boundary condition. We perform steady-state isothermal simulations as the top contact is biased to 2 V and the I-V curves are traced.

We expect to see the effects of the sheet resistance of the contact metal in such large devices, and to model this, we also solve for the vacuum level and Fermi level in the metal. Furthermore, current transport equations in the metal are given by $I_m = -\sigma \cdot \nabla \phi_m$, where σ is the metal conductivity and ϕ_m is the Fermi potential in the metal. As mentioned earlier, the metal/Ga₂O₃ epilayer interface is initialized using the thermionic emission equations while the probe contact on the metal has the Dirichlet boundary condition initialized. In order to simulate different contact metals, the respective conductivity has been used as seen in Table I. Using the basic semiconductor device equations and the above specified metal conductivity equations, the band diagram can be generated as seen in Fig. 3. The band diagrams will help us differentiate between the device under moderate forward bias and strong forward bias, while also highlighting the difference in the thermionic emission current under the probes and at the periphery of the device.

III. RESULTS AND DISCUSSION

A. Experimental

We found that devices up to 1.15 cm² still retained reverse breakdown voltages >240 V, while larger devices typically had

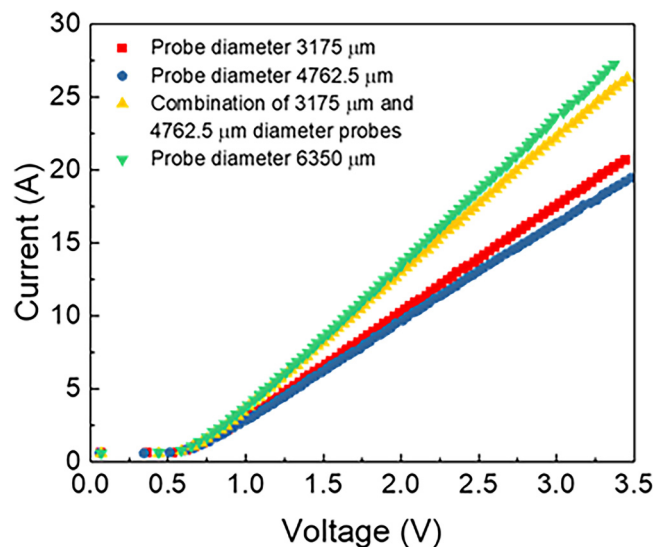


FIG. 4. I-Vs measured on 1.15 cm² rectifiers with circular Al rod probe of different diameters.

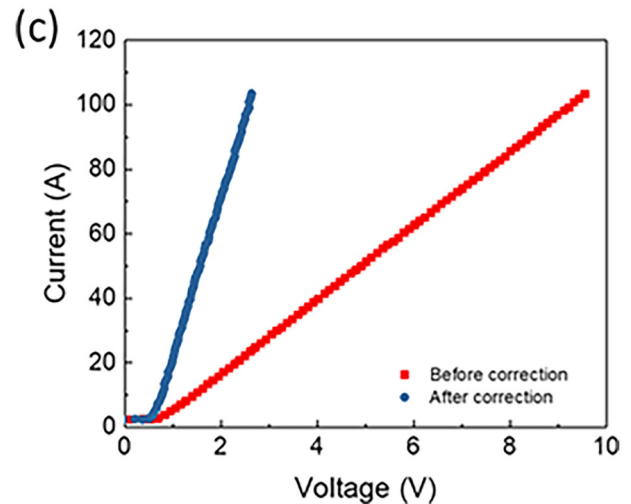
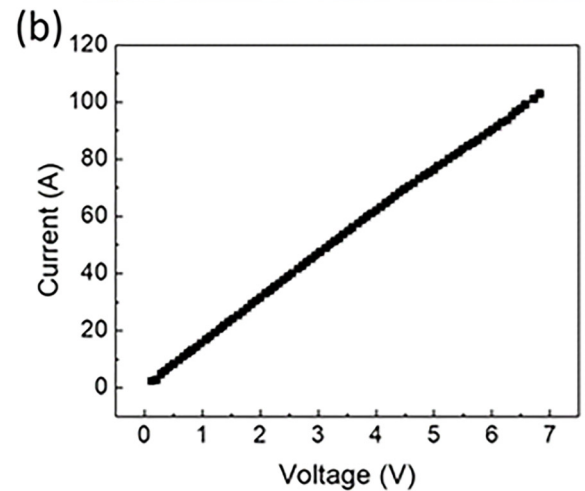
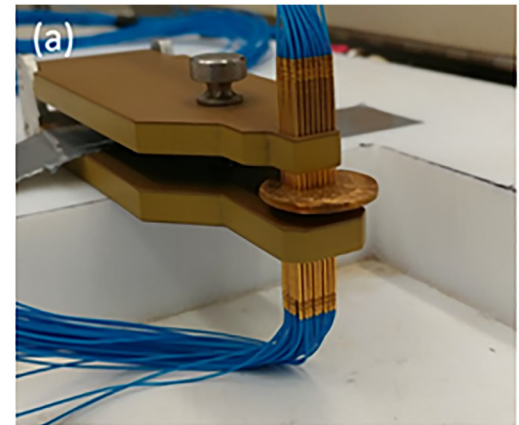


FIG. 5. (a) Microscope image of 6 × 8 arrays of probe tips, covering an area of 48 mm². (b) Short circuit measurement for correcting the parasitic resistance of the probe [probe resistance (0.0669 Ω)]. (c) Single sweep forward current measurement on 1.15 cm² rectifier before and after correction for probe resistance.

breakdown voltages <200 V. This is likely due to the higher probability of including the void defects mentioned earlier within the active region of the rectifier as the area increases.^{54–56} Recent studies have shown that screw and mixed dislocations with an

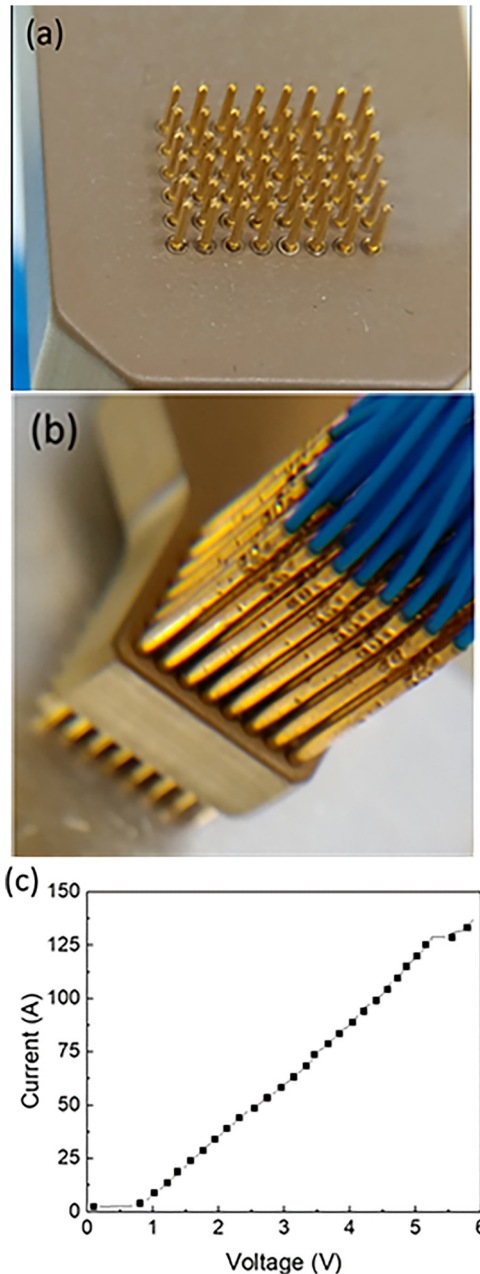


FIG. 6. Images of (a) multiple-tip probe with pad size $6 \times 8 \text{ mm}^2$. (b) Probe connection through the plastic holder. (c) Forward I-V single sweep showing a maximum current of ~ 135 A.

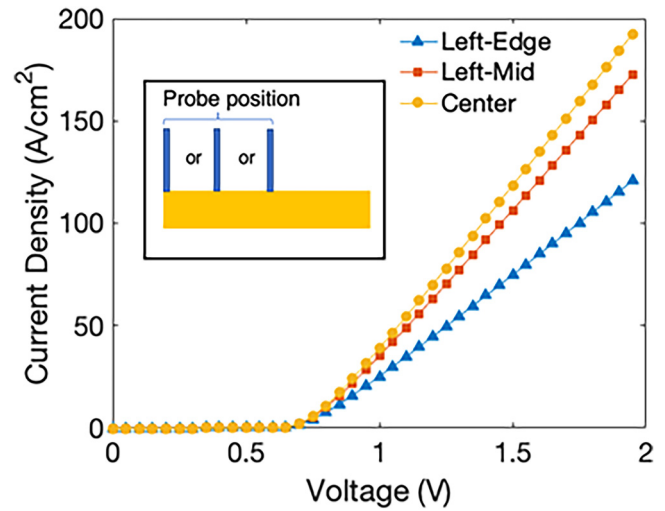


FIG. 7. Current density-voltage (J-V) characteristic as a function of probe position along the surface ($5000 \mu\text{m}$ diameter rectifier), with probe diameter fixed at $40 \mu\text{m}$.

average density of $\sim 10^4 \text{ cm}^{-2}$ and grain boundaries exist in these substrates, even after chemical mechanical polishing of the epilayer.⁵⁶ Examples of the single sweep forward and reverse I-V characteristics of a 1.15 cm^2 area rectifier are shown in Figs. 1(c) and 1(d), respectively. These were measured with a single probe in the form of an Al rod with diameter $3175 \mu\text{m}$ (0.3175 cm). This device was from near the center of the original wafer, shown as the $7545 \times 15245 \mu\text{m}$ device in Fig. 1(b). A drawback with

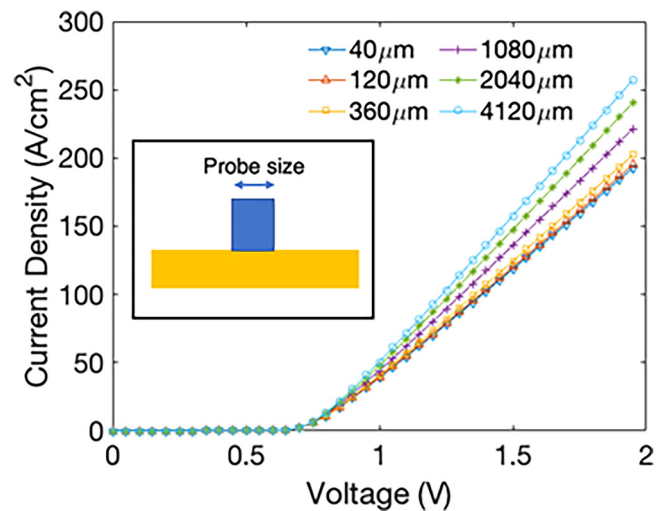


FIG. 8. J-V characteristic as a function of probe diameter, with probe position fixed at the center of the rectifier contact.

using these single rods as measurement probes is the difficulty in ensuring the full area of the rod contacts the device contact on a microscopic level. Our results show that in the present state-of-the-art Ga_2O_3 vertical rectifier structures, it is still a balancing act in terms of increasing device area while maintaining acceptable electrical performance.^{38,39} It is imperative to reduce the current density in the rectifiers below the threshold for thermally driven degradation. Device failure is dependent on the rectifier area and geometry and is generally observed when the junction temperature exceeds $\sim 270\text{--}350^\circ\text{C}$, corresponding to current densities of $185\text{--}2000\text{ A cm}^2$. Previous reports have shown that the inability to dissipate the heat in Ga_2O_3 produces mechanical failure of the material along natural cleavage planes.⁵⁴

We noticed that the maximum forward current we could achieve did not scale with device area, suggesting that current

spreading is an issue in the larger devices. Figure 4 shows the single sweep forward I-Vs in the low-voltage regime from the 1.15 cm^2 rectifier measured with different probe diameters ($0.3175\text{--}0.635\text{ cm}$) and with two probes totaling 0.794 cm diameter placed about 0.5 cm apart. It is clear that the measured current increases with probe diameter, but two probes do not bring the expected linear increase in current.

We then measured the devices with the probe array shown in Fig. 5(a), with 48 probes within a 48 mm^2 area. To obtain the total probe resistance, Fig. 5(b) shows the setup for a short circuit measurement to obtain the parasitic resistance of the probe arrays. An Au-plated copper plate was employed as a short circuit and the probe resistance extracted from the resultant I-V characteristics. This was obtained as $0.0673\ \Omega$. Apparent forward currents from 28 A

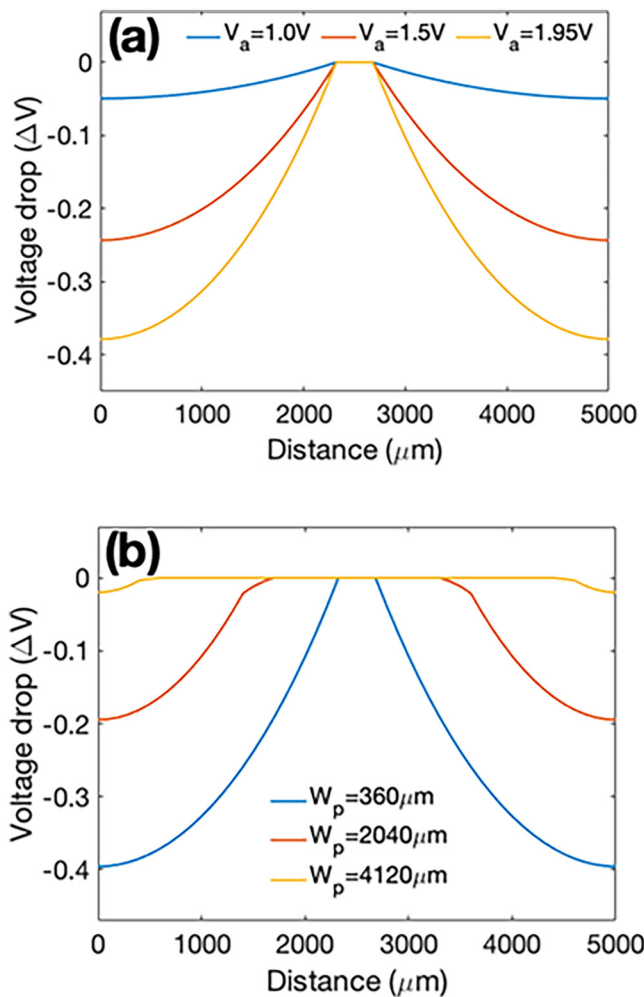


FIG. 9. Voltage drop across the metal/ $\beta\text{-Ga}_2\text{O}_3$ interface for a $5000\ \mu\text{m}$ diameter rectifier (a) at 1.0, 1.5, and 1.95 V of forward bias for a probe size of $360\ \mu\text{m}$, and (b) for different probe sizes.

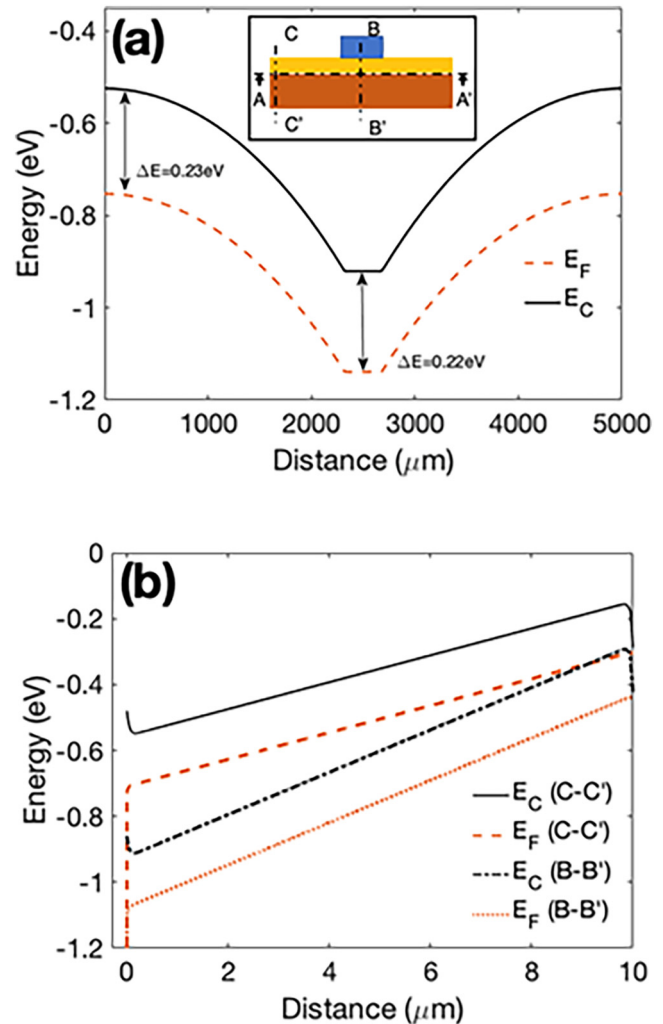


FIG. 10. Conduction band level and Fermi level at (shown in inset) (a) the lateral cut line A-A', and (b) the vertical cut lines B-B' and C-C'.

for 1.15 cm^2 to 14 A for 0.035 cm^2 diodes for voltages $<3 \text{ V}$ were obtained prior to probe resistance correction. However, Fig. 5(c) shows the current sweep before and after correction of this resistance for the 1.15 cm^2 devices, with a significantly higher current when corrected for the probe resistance.

Figures 6(a) and 6(b) show more detailed images of the probe array, while Fig. 6(c) shows the maximum forward current of $\sim 135 \text{ A}$ we obtained while staying below the threshold for device failure. Since these are only single sweep results, more detailed studies are needed of the duty cycle dependence and switching characteristics of these large area devices. Many advances in thermal management approaches in Ga_2O_3 devices have recently been reported,^{57–62} and it is likely that cooling methods developed for GaN can be used for Ga_2O_3 .

B. Simulation

We investigated the geometrical effects of the measurement probe setup in terms of the width of the probe, position of the probe contact on the metal, single- versus multiprobe systems, and different contact metals. We also analyzed the voltage drop measured across the metal- Ga_2O_3 interface to correlate the potential drop to the on-state resistance of the device. Figure 7 shows the current-voltage characteristics of the device with the probe placed on the metal at different positions (seen the inset in Fig. 7) along the diameter. As the probe is moved toward the center of the device, the on-resistance of the device decreases ($0.039\text{--}0.024 \Omega$), which can be attributed to the sheet resistance of the metal layer. When the probe position is near the periphery, the resistance of the metal layer is maximum as the voltage is dropped laterally over the width, i.e., $5000 \mu\text{m}$; however, when the probe is placed at the center, the resistance is minimized as the voltage drops over half of the width, i.e., $2500 \mu\text{m}$. The size of the probe has been studied

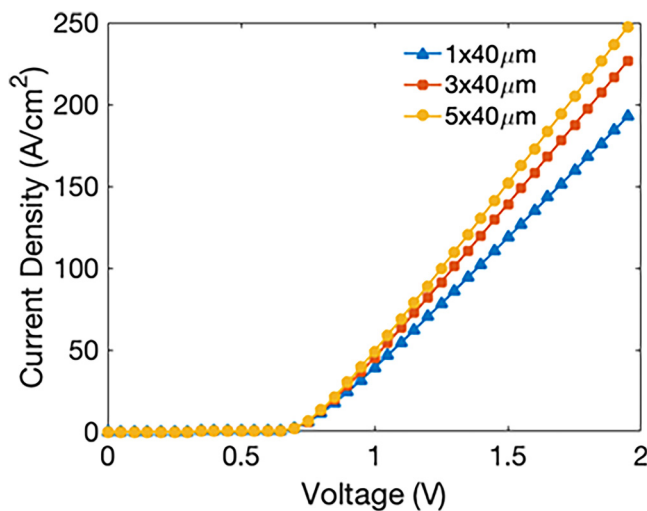


FIG. 11. Current density-voltage curve traced for the device with a measurement probe setup consisting of one, three, or five $40 \mu\text{m}$ wide probes with a constant S_p ($600 \mu\text{m}$).

next, and Fig. 8 shows the current-voltage characteristics of the device with different probe sizes, as depicted in the inset of the figure. The device on-resistance decreases from 0.0236Ω for a probe wise of $40 \mu\text{m}$ to 0.0176Ω for a probe size of $4120 \mu\text{m}$. The wider the probe, the larger the equipotential area under the probe, and hence lower the lateral voltage drop along the metal layer. This can be seen in Fig. 9(a) where we plot the voltage drop across the metal/ Ga_2O_3 interface for different probe sizes. Figure 9(b) gives the lateral voltage drop at different forward biases for a probe size of $360 \mu\text{m}$ showing the increase in voltage drop as the biased is increased, which also denotes a higher lateral current flux in the metal layer.

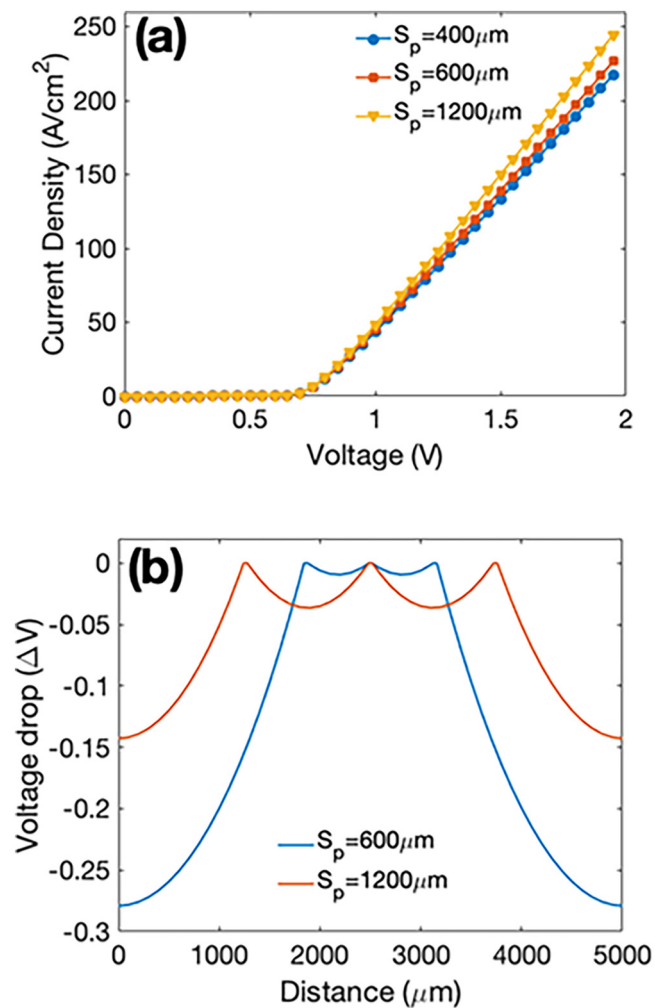


FIG. 12. (a) Forward current density-voltage curve traced for the device with a measurement probe setup consisting of three probes spaced apart by 400 , 600 , or $1200 \mu\text{m}$. (b) Voltage drop across the metal/ $\beta\text{-Ga}_2\text{O}_3$ interface as a function of probe spacing, S_p .

Figure 10 shows the conduction band and Fermi level at the three cut lines, one laterally (A–A') across the metal/Ga₂O₃ interface as seen in Fig. 10(a) and two vertical cut lines at the center (B–B') and periphery of the device (C–C') as seen in Fig. 10(b). The figures represent a device with the probe size of 360 μm biased to 1.95 V. The current flux can be visualized in these figures through the slope of the conduction band. Figure 10(a) also shows that ΔE ($E_C - E_F$) is larger toward the periphery of the device resulting in a higher carrier concentration in the center of the device (under the probe). Furthermore, the magnitude of the thermionic emission can qualitatively be estimated to be larger at the center of the device as opposed to the edge of the device. From Fig. 10(b), we can see that the slope of the conduction band is higher at the central cut line resulting in a higher vertical current flux at the center than at the periphery of the device.

The measurement probe setup can be modified into a multiprobe setup where multiple probes can form contacts with the metal, which would help reduce the sheet resistance effects of the thin metal layer. The number of probes and the spacing between the probes have been analyzed to help design the most efficient measurement multiprobe setups. Figure 11 shows the effect of increasing the number of probes (N_p) on the I–V characteristics while the spacing (S_p) between consecutive probes is maintained as 600 μm . Figure 12(a) shows the I–V curves of the device simulated with three 40 μm wide probes while S_p is increased from 400 to 1200 μm . We notice that using a larger S_p results in a higher current density, which is represented in terms of potential drop across the metal/Ga₂O₃ interface in Fig. 12(b). In order to show the combined effect, the device is then simulated with $N_p = 2, 3$, and 5, while the distance between the two peripheral probes is kept constant at 2520 μm , as seen in the inset of Fig. 13. As the number of probes in increased, the voltage drop between consecutive probes

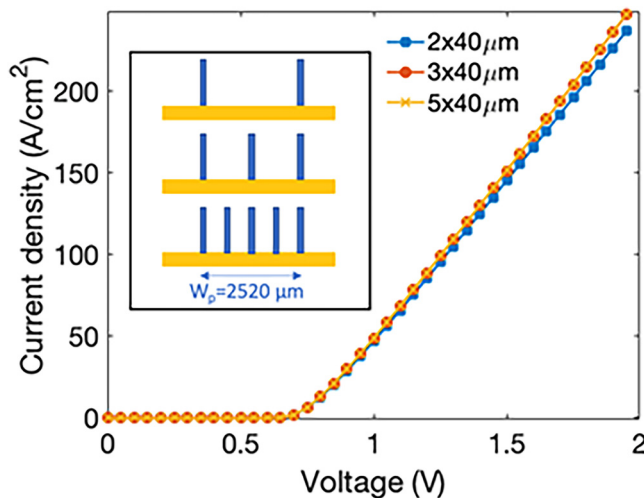


FIG. 13. Forward current density-voltage curve traced for the device with a measurement probe setup consisting of two, three, or five 40 μm wide probes with W_p constant at 2520 μm .

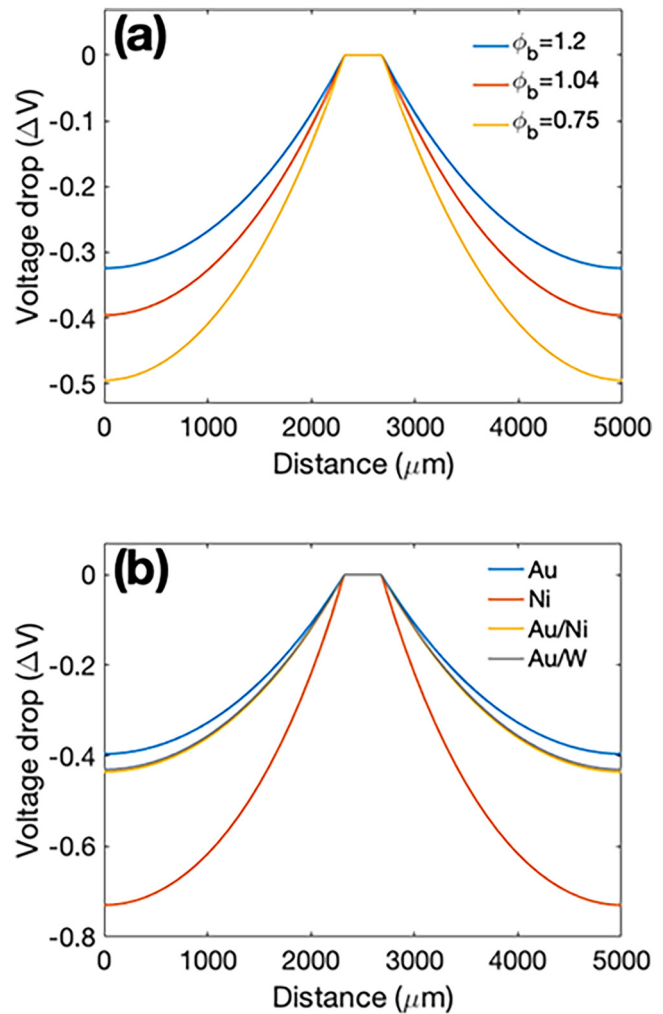


FIG. 14. Voltage drop across the metal/ β -Ga₂O₃ interface for a 5000 μm diameter rectifier with a probe size of 360 μm (a) as a function of the Schottky barrier height and (b) as a function of the different contact metals.

reduces resulting in a slightly lower resistance. The on-resistance of the device decreases by 4.3% when five probes are used over a distance of 2520 μm instead of two probes.

The device is also simulated with different Schottky contact metals in order to analyze the I–V characteristics and the lateral voltage drop. As the SBH is increased, the turn-on voltage increases resulting in lower current density corresponding to the applied voltage, which results in lower lateral voltage drops as seen in Fig. 14(a). Figure 14(b) shows the lateral voltage drop for different contact metal conductivities (Table I). Nickel has a lower conductivity and hence we see the highest lateral voltage drop for a Ni/ β -Ga₂O₃ diode; however, gold has been used as an extra layer to lower the sheet resistance of the contact metal resulting in a lower on-resistance of the device.

IV. SUMMARY AND CONCLUSIONS

A combined experimental and simulation study has been used to understand the effect of probe dimensions and geometry on the current-voltage characteristics of large area Ga₂O₃ rectifiers. The resistance of the probe and the sheet resistance of the Schottky contact means that the measured I-V characteristics must be corrected to obtain the true current. Employing a large number of probes with an area that is significantly relative to the rectifier contact dimensions produces a current of ~135 A on large area (1.15 cm²) devices. Thermal management under switching conditions for these large currents will be the next issue to address. An additional factor that will help in realizing the true potential of Ga₂O₃ for high power rectifiers is the use of higher Schottky barrier height metals. It has recently been shown that larger barrier heights will allow larger breakdown fields,¹⁹ while oxidized metal contacts such as PtO_x, RuO_x, and IrO_x have been demonstrated to have barrier heights up to 2 eV.⁶³

ACKNOWLEDGMENTS

The work at UF was sponsored by the Department of the Defense, Defense Threat Reduction Agency (No. HDTRA1-17-1-011) (J. Calkins) and DTRA Interaction of Ionizing Radiation with Matter University Research Alliance (Award No. HDTRA1-20-2-0002) (J. Calkins). The content of the information does not necessarily reflect the position or the policy of the federal government, and no official endorsement should be inferred. The work is also sponsored by NSF (No. DMR 1856662) (James Edgar). Research at NRL was supported by the Office of Naval Research (ONR).

DATA AVAILABILITY

The data that support the findings of this study are available within the article.

REFERENCES

- ¹H. Masataka, S. Kohei, M. Hisashi, K. Yoshinao, K. Akinori, K. Akito, M. Takekazu, and Y. Shigenobu, *Semicond. Sci. Technol.* **31**, 34001 (2016).
- ²Hongpeng Zhang, Lei Yuan, Xiaoyan Tang, Jichao Hu, Jianwu Sun, Yimen Zhang, Yuming Zhang, and Renxu Jia, *IEEE Trans. Power Electron.* **35**, 5157 (2020).
- ³S. J. Pearton, J. Yang, P. H. Carey IV, F. Ren, J. Kim, M. J. Tadjer, and M. A. Mastro, *Appl. Phys. Rev.* **5**, 011301 (2018).
- ⁴Z. Galazka, *Semicond. Sci. Technol.* **33**, 113001 (2018).
- ⁵Elaheh Ahmadi and Y. Oshima, *J. Appl. Phys.* **126**, 160901 (2019).
- ⁶Xuan Huang, Fei Liao, Ling Li, Xiao Liang, Qiang Liu, Chaoqun Zhang, and Xintong Hu, *ECS J. Solid State Sci. Technol.* **9**, 045012 (2020).
- ⁷M. Higashiwaki and G. H. Jessen, *Appl. Phys. Lett.* **112**, 060401 (2018).
- ⁸Hang Dong, Guangwei Xu, Xuanze Zhou, Wenhao Xiong, Xueqiang Xiang, Weibing Hao, Shibing Long, and Ming Liu, "β-Ga₂O₃ power field effect transistors," in *Wide Bandgap Semiconductor-Based Electronics*, edited by F. Ren and S. J. Pearton (IOP, Oxford, 2020).
- ⁹S. J. Pearton, F. Ren, M. Tadjer, and J. Kim, *J. Appl. Phys.* **124**, 220901 (2018).
- ¹⁰Jiaye Zhang, Jueli Shi, Dong-Chen Qi, Lang Chen, and Kelvin H. L. Zhang, *APL Mater.* **8**, 020906 (2020).
- ¹¹Alex Q. Huang, *IEEE Electron Device Lett.* **25**, 298 (2004).
- ¹²K. Konishi, K. Goto, H. Murakami, Y. Kumagai, A. Kuramata, S. Yamakoshi, and M. Higashiwaki, *Appl. Phys. Lett.* **110**, 103506 (2017).

- ¹³J. Yang, F. Ren, M. Tadjer, S. J. Pearton, and A. Kuramata, *ECS J. Solid State Sci. Technol.* **7**, Q92 (2018).
- ¹⁴Z. Hu *et al.*, *Appl. Phys. Lett.* **113**, 122103 (2018).
- ¹⁵Q. He *et al.*, *IEEE Electron Device Lett.* **39**, 556 (2018).
- ¹⁶W. Li *et al.*, *Appl. Phys. Lett.* **113**, 202101 (2018).
- ¹⁷Jiancheng Yang *et al.*, *Appl. Phys. Lett.* **114**, 232106 (2019).
- ¹⁸W. Li, K. Nomoto, Z. Hu, D. Jena, and H. G. Xing, *IEEE Electron Device Lett.* **41**, 107 (2020).
- ¹⁹W. Li, K. Nomoto, Z. Hu, D. Jena, and H. G. Xing, *IEEE Trans. Electron Devices* **67**, 3938 (2020).
- ²⁰Z. Hu, H. Zhou, Q. Feng, J. Zhang, C. Zhang, K. Dang, and Y. Hao, *IEEE Electron Device Lett.* **39**, 1564 (2018).
- ²¹C. Joishi, S. Rafique, Z. Xia, L. Han, S. Krishnamoorthy, Y. Zhang, S. Lodha, H. Zhao, and S. Rajan, *Appl. Phys. Express* **11**, 031101 (2018).
- ²²W. Li *et al.*, *IEEE International Electron Devices Meeting (IEDM)*, San Francisco, CA, 1–5 December 2018 (IEEE, New York, 2018).
- ²³W. Li, K. Nomoto, Z. Hu, T. Nakamura, D. Jena, and H. G. Xing, *IEDM Technical Digest*, San Francisco, CA, 7–11 December 2019 (IEEE, New York, 2019), pp. 12.4.1–12.4.4.
- ²⁴Chia-Hung Lin *et al.*, *IEEE Electron Device Lett.* **40**, 1487 (2019).
- ²⁵K. Ghosh and U. Singiseti, *J. Appl. Phys.* **24**, 085707 (2018).
- ²⁶J. Yang, F. Ren, M. Tadjer, S. J. Pearton, and A. Kuramata, *AIP Adv.* **8**, 055026 (2018).
- ²⁷Hui Wen Xue, Qi Ming He, Guang Zhong Jian, Shi Bing Long, Tao Pang, and Ming Liu, *Nanoscale Res. Lett.* **13**, 290 (2018).
- ²⁸Ribhu Sharma, Erin E. Patrick, M. E. Law, F. Ren, and S. J. Pearton, *ECS J. Solid State Sci. Technol.* **8**, Q234 (2019).
- ²⁹N. Allen, M. Xiao, X. Yan, K. Sasaki, M. J. Tadjer, J. Ma, R. Zhang, H. Wang, and Y. Zhang, *IEEE Electron Device Lett.* **40**, 1399 (2019).
- ³⁰M. H. Wong, K. Sasaki, A. Kuramata, S. Yamakoshi, and M. Higashiwaki, *IEEE Electron Device Lett.* **37**, 212 (2016).
- ³¹Ke Zeng, Abhishek Vaidya, and Uttam Singiseti, *Appl. Phys. Express* **12**, 081003 (2019).
- ³²Y. Gao *et al.*, *Nanoscale Res. Lett.* **14**, 8 (2019).
- ³³Zahabul Islam, Aman Haque, Nicholas R. Glavin, Minghan Xian, Fan Ren, Alexander Y Polyakov, Anastasia I. Kochkova, Marko Tadjer, and S. J. Pearton, *ECS J. Solid State Sci. Technol.* **9**, 055008 (2020).
- ³⁴Z. Xia, Hareesh Chandrasekar, Wyatt Moore, Caiyu Wang, Aidan J. Lee, Joe McGlone, Nidhin Kurian Kalarickal, Aaron Arehart, and Steven Ringel, *Appl. Phys. Lett.* **115**, 252104 (2019).
- ³⁵Wenshen Li, Devansh Saraswat, Yaoyao Long, Kazuki Nomoto, Debdeep Jena, and Huili Grace Xing, *Appl. Phys. Lett.* **116**, 192101 (2020).
- ³⁶Z. Hu *et al.*, *IEEE Electron Device Lett.* **41**, 441 (2020).
- ³⁷Mark Hollis, O. Slobodyan, J. Flicker, J. Dickson, A. Binder, T. Smith, and Robert Kaplar, *2020 MRS Virtual Spring/Fall Meeting & Exhibit*, Boston, MA, Dec 2020 (Materials Research Society, Warrendale, PA, 2020).
- ³⁸Zahabul Islam, Minghan Xian, Aman Haque, Fan Ren, Marko Tadjer, Nicholas Glavin, and S. J. Pearton, *IEEE Trans. Electron Devices* **67**, 3056 (2020).
- ³⁹M. Xian, C. Fares, F. Ren, Z. Islam, A. Haque, M. Tadjer, and S. J. Pearton, *ECS J. Solid State Sci. Technol.* **9**, 035007 (2020).
- ⁴⁰Leidang Zhou, Xing Lu, Liang Chen, Xiaoping Ouyang, Bo Liu, Jun Xu, and Huili Tang, *ECS J. Solid State Sci. Technol.* **8**, Q3054 (2019).
- ⁴¹H. H. Gong, X. H. Chen, Y. Xu, F.-F. Ren, S. L. Gu, and J. D. Ye, *Appl. Phys. Lett.* **117**, 022104 (2020).
- ⁴²Jiancheng Yang, Chaker Fares, Randy Elhassani, Minghan Xian, Fan Ren, S. J. Pearton, Marko Tadjer, and Akito Kuramata, *ECS J. Solid State Sci. Technol.* **8**, Q3159 (2019).
- ⁴³Yuangang Wang *et al.*, *IEEE Electron Device Lett.* **41**, 131 (2020).
- ⁴⁴Masaya Oda, Rie Tokuda, Hitoshi Kambara, Tomochika Tanikawa, Takahiro Sasaki, and Toshimi Hitora, *Appl. Phys. Express* **9**, 021101 (2016).
- ⁴⁵Kentaro Kaneko, Shizuo Fujita, and Toshimi Hitora, *Jpn. J. Appl. Phys.* **57**, 02CB18 (2018).

- ⁴⁶Kentaro Kaneko, *J. Soc. Mater. Sci. Jpn.* **66**, 58 (2017).
- ⁴⁷A. Segura, L. Artús, R. Cuscó, R. Goldhahn, and M. Feneberg, *Phys. Rev. Mater.* **1**, 024604 (2017).
- ⁴⁸E. B. Yakimov *et al.*, *APL Mater.* **8**, 111105 (2020).
- ⁴⁹E. B. Yakimov *et al.*, *J. Phys. D Appl. Phys.* **53**, 495108 (2020).
- ⁵⁰Sayleap Sdoeung, Kohei Sasaki, Katsumi Kawasaki, Jun Hirabayashi, Akito Kuramata, Toshiyuki Oishi, and Makoto Kasu, *Appl. Phys. Lett.* **117**, 022106 (2020).
- ⁵¹M. E. Law and S. M. Cea, *Comput. Mater. Sci.* **12**, 289 (1998).
- ⁵²S. M. Sze and K. N. Kwok, *Physics of Semiconductor Devices* (Wiley, New York, 2006).
- ⁵³S. K. Cheung and N. W. Cheung, *Appl. Phys. Lett.* **49**, 85 (1986).
- ⁵⁴M. Ahn, A. Sarracino, A. Ansari, B. Torralva, S. Yalisove, and J. Phillips, *J. Appl. Phys.* **125**, 223104 (2019).
- ⁵⁵Minghan Xian, Randy Elhassani, Chaker Fares, Fan Ren, Marko Tadjer, and S. J. Pearton, *J. Vac. Sci. Technol. B* **37**, 061205 (2019).
- ⁵⁶Hiroataka Yamaguchi, Shinya Watanab, Yu Yamaoka, Kimiyoshi Koshi, and Akito Kuramata, *Jpn. J. Appl. Phys.* **59**, 125503 (2020).
- ⁵⁷Takashi Matsumae, Yuichi Kurashima, Hitoshi Umezawa, Koji Tanaka, Toshimitsu Ito, Hideyuki Watanabe, and Hideki Takagi, *Appl. Phys. Lett.* **116**, 141602 (2020).
- ⁵⁸Chao Yuan, Yuewei Zhang, Robert Montgomery, Samuel Kim, Jingjing Shi, Akhil Mauze, Takeki Itoh, James S. Speck, and Samuel Graham, *J. Appl. Phys.* **127**, 154502 (2020).
- ⁵⁹J. W. Pomeroy *et al.*, *IEEE Electron Device. Lett.* **40**, 189 (2019).
- ⁶⁰R. Sharma, E. Patrick, M. E. Law, J. Yang, F. Ren, and S. J. Pearton, *ECS J. Solid State Sci. Technol.* **8**, Q3195 (2019).
- ⁶¹James Spencer Lundh *et al.*, *J. Electron. Packag.* **142**, 031113 (2020).
- ⁶²Bikramjit Chatterjee *et al.*, *Appl. Phys. Lett.* **117**, 153501 (2020).
- ⁶³C. Hou, K. R. York, R. A. Makin, S. M. Durbin, R. M. Gazoni, R. J. Reeves, and M. W. Allen, *Appl. Phys. Lett.* **117**, 203502 (2020).